

Piezoelectric polymer generators: the large bending regime

E. Sarrey, M. Sigallon, M.-C. Clochard, and J.-E. Wegrowe*

*Laboratoire des Solides Irradiés, CEA/DRF/IRAMIS, Ecole Polytechnique,
CNRS, Institut Polytechnique de Paris, F-91128, Palaiseau, France*

A.-L. Hamon

*Laboratoire de Mécanique Paris-Saclay,
Université Paris-Saclay, CentraleSupélec,
ENS Paris-Saclay, CNRS F-91190, Gif-sur-Yvette, France*

(Dated: November 8, 2024)

Abstract

There is an important difference between piezoelectric polymer films and solid crystals for the application to piezoelectric generators. In the case of polymers, the optimal piezoelectric response imposes a *large bending regime*. Starting from the linear Curie's constitutive equations, we develop an analytical model under the assumption of the large bending regime resulting from bulge testing configuration. This model shows a specific non-linear piezoelectric response, that follows a power $2/3$ of the mechanical excitation. The piezoelectric voltage and the corresponding power are then studied experimentally as a function of the angular frequency ω of the mechanical excitation, the load resistance R , and the thickness of the film ℓ . The experimental results carried out on piezoelectric PVDF films validate the model.

I. INTRODUCTION

The best way to extract power from a piezoelectric polymer film is to deform it. In contrast, the usual piezoelectric ceramics are not deformable at the macroscopic scale. As a result, the optimization of a polymer piezoelectric generator imposes to work in the large bending regime^{1,2}. The specificity of such a nonlinear regime has been studied by *Mo et al.* in reference³ for PVDF piezoelectric films in the context of energy harvesting. Their method (also used in subsequent works⁴), is based on the equilibrium states (energy minimization). The maximum energy that can be harvested has been given. However, analytical expressions for a time-dependent (or frequency dependent) mechanical excitations, and the corresponding electric power generated in a load circuit, are still to be derived.

The present article is a report of a systematic theoretical and experimental study about the large bending regime and the piezoelectric response to a time-dependent excitation of the PVDF film, contacted to a load circuit. The analysis is performed on the basis of the linear constitutive laws of the Curie brothers.

Due to the tensor nature of the equations, the number of parameters is huge : ten parameters in the case of transversely isotropic films (six for the elasticity tensor, two for the electric permittivity, and two for the piezoelectric coupling). Thus, the equations describe all possible experimental situations with various piezomaterials. In the case of piezoelectric generators, the constraints are reduced to a known external mechanical excitation and a known geometrical disposition of the two electrodes that forms the piezoelectric capacitor (so that the direction of the electrical field \mathbf{E} is known). However, even within these restrictions, the number of possible configurations is still huge, and takes into account small to large deflection regimes.

In the context of energy harvesting at low frequency (non-resonant transducers) with polymer thin films, the main mechanical characteristics are the large transverse displacement (hundreds of micrometers), with respect to the thickness (a few tens of micrometers) for a free standing circular film fixed at the border. In order to derive operational analytical expressions, a “large deflection” model⁵ is used and applied to an experimental investigation performed on PVDF films. The analytical solutions to the problem are studied and compared systematically to the measured voltage and power, both for the frequency and the time domains. It is a common approach to study the output electric power with respect to the

varied load resistance^{6, 7, 8}, however, it is less common to tune it also with the frequency⁹. The experimental study is performed as a function of the frequency ω of the periodic mechanical excitation, the load resistance R of the electric circuit, and the thickness of the piezoelectric film ℓ . The main experimental observations are the following:

1. For fixed material's parameters, the maximum power is reached when $RC\omega = 1$, where R is the resistance of the circuit, ω the frequency, and C is the effective capacitance (impedance matching condition).
2. The ordinary differential equation of the first order in time is not linear in the mechanical excitation. Instead, the Fourier transform of the voltage V_ω is proportional to the Fourier transform of the pressure p_ω at the power of $2/3$.
3. Scaling law: the ratio $V_\omega/(p_\omega^{2/3})$ of V_ω divided by p_ω to the power of $2/3$ is a simple function of the product $R\omega$ (and not a function of the two separate variables R and ω).
4. The typical dependence of the voltage V_ω as a function of the thickness ℓ follows approximately the power law $V_\omega(\ell) \propto \ell^{-2/3}$.

While the first characteristic 1) is well-known (see however the discussion in reference Amiri *et al.*⁹), the properties 2), 3) and 4) are peculiar to the non-linear model presented in the present report. Furthermore, the Figure of Merit of the system¹⁰ is derived for the considered regime.

The paper is composed as follows. After section II that presents briefly the set-up, section III exposes the large bending model, focusing on the four predictions exposed above. Section IV is a report of the experimental results that illustrate the main predictions of the model. The last section V presents a discussion with our conclusions.

II. PIEZOELECTRIC GENERATOR

The system of interest – sketched in Fig. 1 – is composed of a piston powered by an electric motor (not depicted), with a frequency-control and connected to a pressure chamber. The pressure chamber contains the free standing PVDF film with a fixation O-ring and a

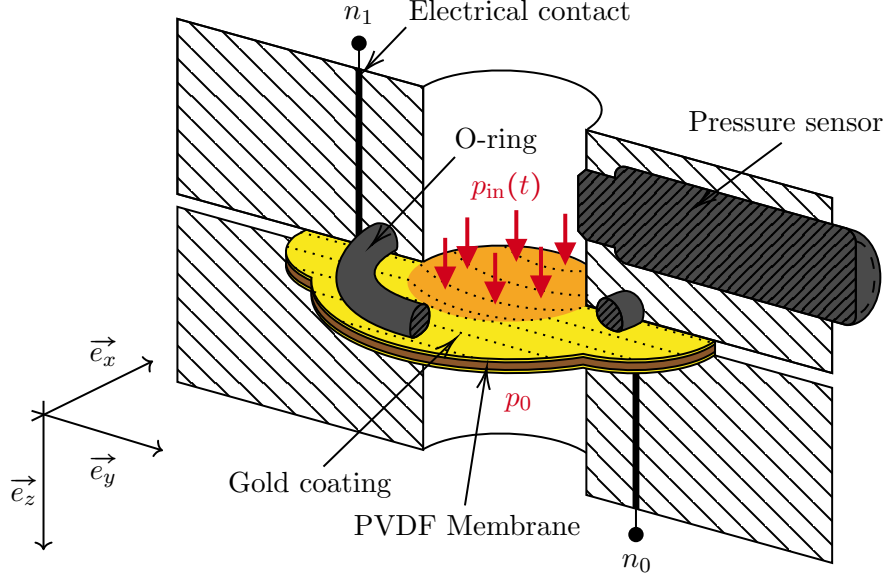


FIG. 1. Illustration of the chamber with (red arrows) the applied pressure $p_{in}(t)$, the atmospheric pressure p_0 , the electric connections, n_0 and n_1 and *in situ* pressure sensor. ■ the electrode area A_e , ■ the pressurized area A_p .

pressure sensor. The film was previously covered by a sputtered gold layer (yellow surface in Fig. 1). It is contacted to the electric load circuit (top n_1 and bottom n_0 electric wires). The electric circuit is composed of a decade resistance box and a voltmeter (not shown). This configuration mimics a real autonomous piezoelectric generator, excited by mechanical vibrations at low frequency, which power is harvested with a small electronic circuit. The low frequency (≤ 32 Hz) is chosen because it should correspond to the vibration frequencies domain of traffic-induced metallic bridge vibrations¹¹, water flows in pipelines¹², human motion for backpack¹³ and textile sensor¹⁴ applications, to name but a few.

As justified below, the optimized system necessitates a bending of the PVDF film resulting in a bulge large with respect to the thickness (hundreds of micrometers vs. tens of micrometers), but small with respect to the lateral sizes of the piezoelectric film (centimetric). The optimized set-up corresponds to this bulge test configuration.

In order to check the role of the large bending on the piezoelectric properties, we used three types of PVDF films with measured thicknesses $\ell=12$, $\ell=28$, and $\ell=116$ μm . The information about the PVDF films are summarized in Appendix A.

The electrodes are typically 50 nm-thick gold layers sputtered on each side of the PVDF

films. Note that the thickness of the electrode will be reconsidered in the discussion and in Appendix B. In the following, A_e denotes the area of each electrode (see Fig. 1). The PVDF film stands freely over a circular hole of 0.8 cm in diameter, and is fixed with O-ring seals on the compression chamber (see Fig. 1). A time-dependent pressure $p_{\text{in}}(t)$ of about 1 bar in magnitude is applied with a piston. The latter motion is controlled by a motor driven by a positioning controller that imposes the time variation of the pressure as close as possible to a sinusoid. The frequency ranges from 3 to 32 Hz: below 3 Hz the output piezoelectric voltage is too small, and above 32 Hz, the signal becomes noisy due to the vibrations induced by the motor on the piston. The pressure is applied on the polymer film over a typical area A_p .

The electrodes are connected to a resistance decade box of resistance R_l , ranging from 10^4 to $10^7 \Omega$. The voltage is measured and recorded on the resistance together with the current, thanks to an analog-to-digital RedPitaya card (ADC). The effective electric circuit simply consists of the piezoelectric generator, the corresponding capacitor of capacity C , the load resistance R_l and the $10^6 \Omega$ resistance R_{rep} of the ADC RedPitaya, the total resistance being $R = R_l R_{rep} / (R_l + R_{rep})$.

III. MODEL

The main objective of this section is to apply the linear Curie's constitutive laws to the geometry of our system (see Fig. 2), and the constraints imposed by our set-up. Indeed, in the present case, the most convenient form of Curie brothers' equations is given by the *Stress-Charge* form¹⁵ (in contrast to the more usual case based on the *Strain-Charge* form):

$$\begin{cases} \mathbf{T} &= \mathbb{C}_E \cdot \mathbf{S} - \mathbf{e}^T \cdot \mathbf{E} \\ \mathbf{D} &= \mathbf{e} \cdot \mathbf{S} + \epsilon_S \cdot \mathbf{E} \end{cases} \quad (1)$$

\mathbf{T} [N/m ²]	Stress
\mathbf{D} [C/m ²]	Electric charge density displacement
\mathbf{S} [1]	Strain
\mathbf{E} [N/C]	Electric field
\mathbb{C} [N/m ²]	Elasticity tensor
\mathbf{e} [C/m ²]	Piezoelectric coupling tensor
ϵ [C ² /(N ² .m ²)]	Electric permittivity matrix

The respective subscripts E and S on the elasticity \mathbb{C}_E and the electric permittivity ϵ_S mean that these quantities are respectively measured at a constant and preferably null electric field or strain.

The relation between the piezoelectric coefficient \mathfrak{e} and the more common Strain-Charge piezoelectric coefficient \mathfrak{d} is given by:

$$\mathfrak{e} = \mathfrak{d} \cdot \mathbb{C}_E. \quad (2)$$

In our specific case, taking into account the setup axisymmetric geometry and the properties of the transversely isotropic polymer film in the plane:

- \mathbf{T} and \mathbf{S} are reduced to their radial and orthoradial components (no shear);
- \mathbf{D} and \mathbf{E} are reduced to their z component,

so that the set of equations (1) are reduced to the following set of three equations:

$$\begin{aligned} T_{rr} &= \frac{Y}{1-\nu^2} (S_{rr} + \nu S_{\varphi\varphi}) - e_{31} E_z, \\ T_{\varphi\varphi} &= \frac{Y}{1-\nu^2} (\nu S_{rr} + S_{\varphi\varphi}) - e_{31} E_z, \\ D_z &= e_{31} (S_{rr} + S_{\varphi\varphi}) + \epsilon_{33} E_z, \end{aligned} \quad (3)$$

where Y and ν derive from the elasticity tensor and stand respectively for the membrane Young's modulus and Poisson's ratio, and T , S , and D_z are functions of r , z , and t , and the electric field E_z is a function of t alone. From the tensor relation (2) we infer the scalar relation:

$$e_{31} = Y \frac{d_{31} + \nu d_{33}}{(1+\nu)(1-2\nu)}. \quad (4)$$

A periodic pressure functional: $p_{\text{in}}(t) = p_0 + \delta p(t)$ is applied on a film of thickness ℓ . The frequency being far smaller than the eigen-frequency of the film (a maximum of 30 Hz versus a first resonance mode around 350 Hz), a quasi-static approach is used for the mechanical analysis of the system.

For a thin film such as ours, the kinematics consists in decoupling the middle plane ($z = 0$) from the thickness ($-\ell/2 \leq z \leq \ell/2$), and each segment along the z -axis remains locally orthogonal to the middle plane during the transformation, so that the displacement field along the z -axis depends only of the plane coordinates (only r in an axisymmetric problem).

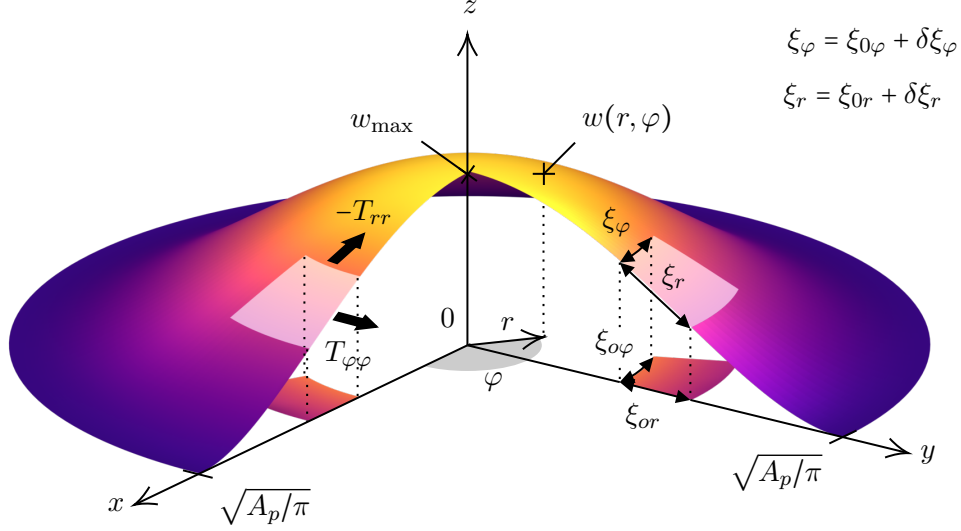


FIG. 2. Transformation of a circular membrane of radius $\sqrt{A_p/\pi}$ due to an overpressure δp . Cylindrical coordinates (r, φ, z) are used. w stands for the z -component of the displacement field for any point of polar coordinates (r, φ) , and w_{\max} its maximum value reached at the center $r = 0$. As a consequence, each radial (resp. orthonormal) segment of length ξ_{0r} (resp. $\xi_{0\varphi}$) is transformed into a segment of length $\xi_r = \xi_{0r} + \delta\xi_r$ (resp. $\xi_\varphi = \xi_{0\varphi} + \delta\xi_\varphi$), so that $S_{rr} = \delta\xi_r/\xi_{0r}$ (resp. $S_{\varphi\varphi} = \delta\xi_\varphi/\xi_{0\varphi}$). The stress components T_{rr} and $T_{\varphi\varphi}$ correspond to the internal force densities applied in the radial and orthonormal directions.

In the case of small bending, the strain is uniformly null on the middle plane, so that the strain is symmetric on each side of the middle plane. From Curie's laws, the strain contribution on D_z is an odd function with respect to the variable z , and there is no effective capacitor. Hence the need to apply an overpressure high enough for large bending $\sqrt{A_p/\pi} > w_{\max} > \ell$ so that the strain is not a linear but an affine function of z . A good analytical expression of the stress in the middle plane, from which the strain can be inferred, is provided in Dedkova *et al.*⁵. Adding the contribution of the z variable, the strain field with respect to the position in the membrane cross-section is null for $r > \sqrt{A_p/\pi}$, and otherwise, for $r \leq \sqrt{A_p/\pi}$:

$$\begin{aligned}
S_{rr}(r, z, t) &\approx S(t) \left(1 - \frac{1-3\nu}{3-\nu} \pi \frac{r^2}{A_p} \right) - z \frac{d^2 w}{dr^2}, \\
S_{\varphi\varphi}(r, z, t) &\approx S(t) \left(1 - \pi \frac{r^2}{A_p} \right) - \frac{z}{r} \frac{dw}{dr},
\end{aligned} \tag{5}$$

with:

$$S(t) = \left(\frac{A_p}{\pi \ell^2} \right)^{\frac{1}{3}} \left(\frac{3}{8} \frac{1-\nu}{7-\nu} \frac{\delta p(t)}{Y} \right)^{\frac{2}{3}} (3-\nu),$$

and where the z -component of the displacement w (see Fig. 2) is given by⁵:

$$w(r, t) = \underbrace{\left(3 \frac{1-\nu}{7-\nu} \frac{A_p^2}{\pi^2 \ell} \frac{\delta p(t)}{Y} \right)^{\frac{1}{3}}}_{w_{\max}(t)} \left(1 - \pi \frac{r^2}{A_p} \right)^2.$$

The surface density of charge on the interface with each electrode ($z = \pm \ell/2$) can be thus found from eq. (3), and is given in eq. (6).

$$D_z \left(r, \pm \frac{\ell}{2}, t \right) \simeq \begin{cases} e_{31} \left[\frac{1-\nu}{2} \left(\frac{A_p}{\pi \ell^2} \right)^{\frac{1}{3}} \left(3 \frac{1-\nu}{7-\nu} \frac{\delta p(t)}{Y} \right)^{\frac{2}{3}} \left(\frac{3-\nu}{1-\nu} - 2\pi \frac{r^2}{A_p} \right) \mp \frac{\ell}{2} \left(\frac{d^2 w}{dr^2} + \frac{1}{r} \frac{dw}{dr} \right) \right] + \epsilon_{33} E_z(t) \\ \text{if } r \leq \sqrt{\frac{A_p}{\pi}} \\ \epsilon_{33} E_z(t) \quad \text{otherwise.} \end{cases} \tag{6}$$

One can then take the surface average over A_e (denoted $\overline{\bullet}$) and get:

$$\overline{D_z} \left(\pm \frac{\ell}{2}, t \right) = \frac{A_p}{A_e} e_{31} \left(\frac{A_p}{\pi \ell^2} \right)^{\frac{1}{3}} \left(3 \frac{1-\nu}{7-\nu} \frac{\delta p(t)}{Y} \right)^{\frac{2}{3}} + \epsilon_{33} E_z(t). \tag{7}$$

since, on average:

$$\overline{\frac{\partial^2 w}{\partial r^2} + \frac{1}{r} \frac{\partial w}{\partial r}} = 0.$$

Now we can use the following relations:

$$E_z(t) = -\frac{V(t)}{\ell}, \quad \text{and} \quad \overline{\dot{D}_z}(t) = \frac{I(t)}{A_e}, \tag{8}$$

where V is the voltage, I the current measured on the resistance, and $\dot{D}_z = \partial D_z / \partial t$ is the time derivative of the electric displacement. Eq. (7) can then be reduced to:

$$I(t) = -C \frac{dV}{dt} + A_p e_{31} \left(\frac{A_p}{\pi \ell^2} \right)^{\frac{1}{3}} \left(3 \frac{1-\nu}{7-\nu} \right)^{\frac{2}{3}} \frac{d}{dt} \left[\left(\frac{\delta p}{Y} \right)^{\frac{2}{3}} \right], \tag{9}$$

where we recognized the capacitance at constant or null strain:

$$C = \frac{\epsilon_{33}A_e}{\ell}. \quad (10)$$

We can then consider our full circuit where R is the equivalent resistance of the load resistance coupled to measurement instrumentation. According to Ohm's law:

$$V = RI. \quad (11)$$

In this case, R corresponds to the equivalent resistance and does not depend on the excitation frequency (assuming no other capacitance in the circuit). Hence, we have:

$$V(t) + RC \frac{dV}{dt} = A_p e_{31} R \left(\frac{A_p}{\pi \ell^2} \right)^{\frac{1}{3}} \left(3 \frac{1-\nu}{7-\nu} \frac{1}{Y} \right)^{\frac{2}{3}} \frac{d}{dt} \left[\left(\frac{\delta p}{Y} \right)^{\frac{2}{3}} \right]. \quad (12)$$

Eq. (12) is an ordinary differential equation (ODE) for a driven RC circuit, for which the driven force is the time-derivative of the pressure to the power of 2/3. An analytical solution of eq. (12) can easily be obtained as a function of frequency after performing a Fourier transform.

A. Analytical result in the frequency domain

The solution of the ODE (12) can be more conveniently manipulated in the frequency space. Indeed, taking, the Fourier transform of eq. (12), we get:

$$\hat{V}(\omega) (1 + iRC\omega) = A_p e_{31} R \left(\frac{A_p}{\pi \ell^2} \right)^{\frac{1}{3}} \left(3 \frac{1-\nu}{7-\nu} \frac{1}{Y} \right)^{\frac{2}{3}} i\omega \mathcal{F}_t \left[\delta p^{\frac{2}{3}}(t) \right] (\omega), \quad (13)$$

with \mathcal{F}_t the Fourier transform operator and $\hat{V}(\omega) = \mathcal{F}_t[V(t)](\omega)$. To conclude, we have:

$$\hat{V}(\omega) = -\mathcal{A}(\ell) \frac{R\omega}{i - RC\omega} \mathcal{F}_t \left[\delta p^{\frac{2}{3}}(t) \right] (\omega), \quad (14)$$

with the *prefactor*:

$$\mathcal{A}(\ell) := A_p e_{31} \left(\frac{A_p}{\pi \ell^2} \right)^{\frac{1}{3}} \left(3 \frac{1-\nu}{7-\nu} \frac{1}{Y} \right)^{\frac{2}{3}}. \quad (15)$$

The amplitude of the voltage is given by the modulus of the complex number Eq.(14):

$$|\hat{V}(\omega)| = \mathcal{A}(\ell) \left| \mathcal{F}_t \left[\delta p^{\frac{2}{3}}(t) \right] (\omega) \right| \frac{R\omega}{\sqrt{1 + (RC\omega)^2}}. \quad (16)$$

As can be seen, Eq. (16) is a scaling law showing that the voltage is a function of the product $R\omega$.

B. Analytical result for the electric power delivered by the generator

The apparent electric power P_e delivered by the piezoelectric generator is by definition $|V|^2/(2R)$, or

$$P_e(R, \omega) = \frac{1}{2} \mathcal{A}^2(\ell) \left| \mathcal{F}_t \left[\delta p^{\frac{2}{3}}(t) \right] (\omega) \right|^2 \frac{R\omega^2}{1 + (RC\omega)^2} \quad (17)$$

C. Predictions of the model

The expression Eq.(17) is the product of three independent terms. The first is defined by the mechanical intrinsic parameters ν , and Y , the piezoelectric parameter e_{31} , and by the geometrical parameters A_p and ℓ . The second is defined by the frequency dependence of the mechanical excitation only (extrinsic parameter), and the last term is a function of the load resistance R (extrinsic parameter), the frequency (extrinsic parameter), and the permittivity ϵ (intrinsic parameter), through the capacitance C .

The typical resonance shape of the Power, with a maximum, is due to the last term only. The maximum is reached for the condition $RC\omega = 1$. This is the maximum of the power than can be obtained for a fixed set of the internal parameters. This condition is the impedance matching between the piezoelectric generator and the electric circuit. It is an intuitive condition, since it corresponds to the situation for which the charges are injected into the electric circuit at the same rate ($\tau = RC$) as they are produced inside the piezoelectric material ($1/\omega$). In other terms, the load resistance can be adapted to the typical frequency of the mechanical excitation.

Besides, the goal is to find the best piezoelectric material for the generator. We should then look at the material parameters that maximize the prefactor \mathcal{A}^2 of the power Eq.(17), given in Eq.(15). This corresponds to the maximization of the following ratio of the intrinsic parameters:

$$\mathcal{A}^2 \propto e_{31}^2 \left(3 \frac{1-\nu}{7-\nu} \frac{1}{Y} \right)^{\frac{4}{3}}, \quad (18)$$

which defines the *Figure of Merit* of this generator, assuming a given mechanical input.

In summary, eq. (16) and eq. (17) predict the four points listed in the introduction:

1. For fixed material's parameter, the electric power corresponds to the condition of the impedance matching: $RC\omega = 1$;

2. The Fourier transform of the voltage is proportional to the Fourier transform of the pressure to the power of $2/3$.
3. Scaling law: the ratio $V_\omega/(p_\omega^{2/3})$ is a simple function of the product $R\omega$.
4. Eq. (14) and eq. (15) show that the voltage is proportional to the thickness to the power of $-2/3$.

The four properties above are those underlined in the introduction. The last three points are specific to the large bending regime. Note that the voltage is also proportional to the Young's modulus to the power of $-2/3$ for an input pressure modelled as a sine function (but this last feature is more difficult to evidence experimentally).

IV. EXPERIMENTAL RESULTS

The raw data of the voltage are measured by the RedPitaya card as a function of time (time traces). The size of the trace is typically of $2^{14} = 16384$ points measured during about 1 s (this number depends on the frequency). A typical time-trace of the pressure is shown in Fig. 3 (top).

The voltage response trace is measured for each value of the load resistance R_l – eight values ranging from 0.01 to 10 M Ω – and each pressure frequency – also eight values ranging from 8 to 32 Hz. An example of the raw data for the voltage is shown in Fig. 5. The corresponding numerical time-derivative is presented in Fig. 3 (bottom), while the numerical Fourier transform (and its time derivative) is calculated from Fig. 3 (top) and shown in Fig. 4. It can be seen that the time-dependence of the pressure is nearly a sinusoidal signal (about 93% according to the Fourier Transform).

A. Time dependence of the measured voltage

The voltage response measured on the numerical voltmeter is shown in Fig. 5 (black line). In order to exploit the results obtained in section III, the measured pressure is derived numerically with respect to time, and used for the numerical solution (Runge-Kutta) of the differential equation (ODE) derived in §III A. The corresponding function of time is plotted in Fig. 5 (dashed line) and compared to the experimental data (without fitting parameter).

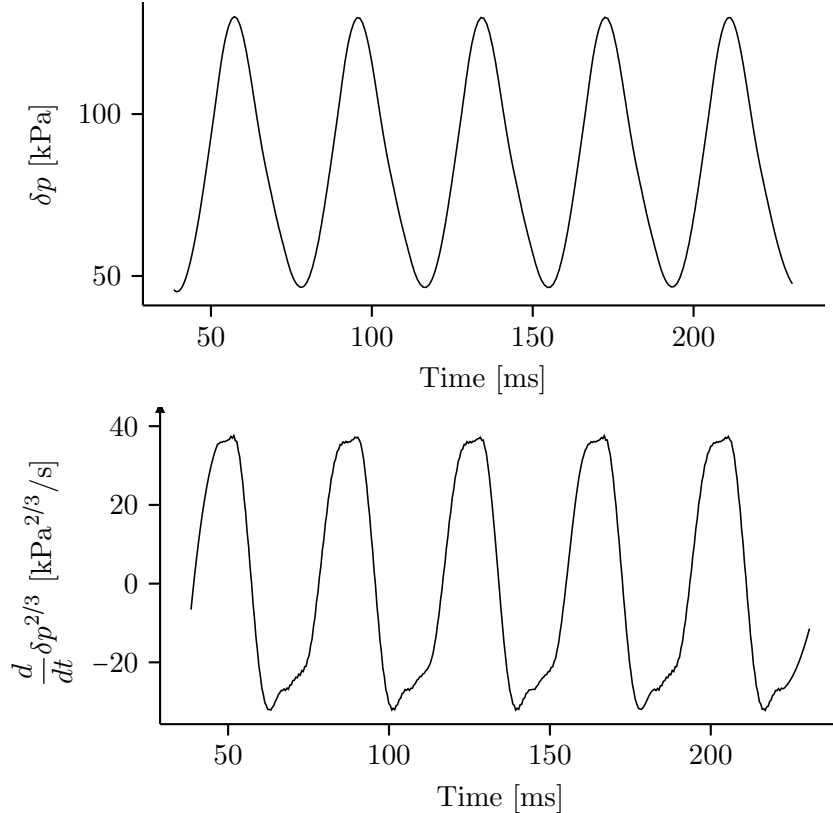


FIG. 3. Top: time trace of the raw input over pressure measurement smoothed using a Savgol filter. The frequency is 26 Hz. Bottom: derivative of the over pressure input to the power of 2/3.

The grey zone accounts for the error bars deduced from the uncertainty of the material's constants given by the manufacturer.

Note that a numerical smoothing was required to prevent spikes in the derivatives which were nonphysical as they were not appearing in the voltage measurement.

As displayed in Fig. 5, this smoothed trace can then be injected into a Runge-Kutta solver to obtain the time trace of the expected voltage for a given pressure trace.

B. Frequency dependence of the measured voltage

The experimental frequency dependence of the voltage is studied using a numerical demodulation algorithm applied to the time-dependent measurements. Figure 6 shows the Fourier transform of the voltage compared with the theoretical model.

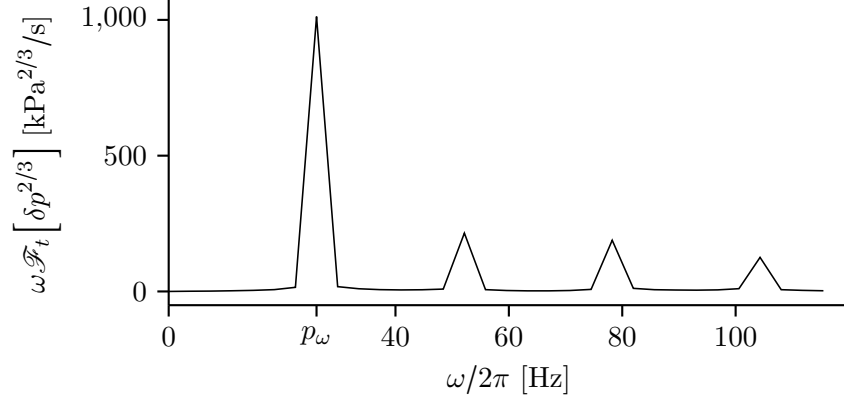


FIG. 4. Numerical Fourier transform (FFT) of the time-derivative of the measured over-pressure to the power of $2/3$. The amplitude of the first peak p_ω is reached for the frequency 26 Hz.

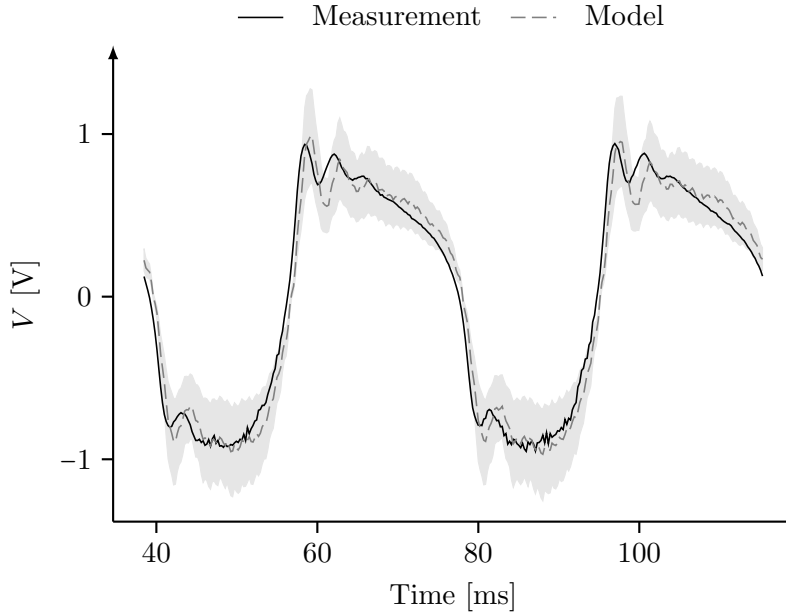


FIG. 5. Time trace of the voltage over a single period. Black line: time trace of the voltage measurements. Dashed line: time trace of the model solved with Runge-Kutta with the uncertainty interval computed using the uncertainty of the material's constants given by the manufacturer. Measurement performed at 26 Hz with 909 k Ω load on the 116 μm -thick sample.

C. Scaling law

The protocol described above is performed at multiple frequencies and multiple load resistances R_l . The measured the voltage divided by the Fourier transform p_ω of the overpressure

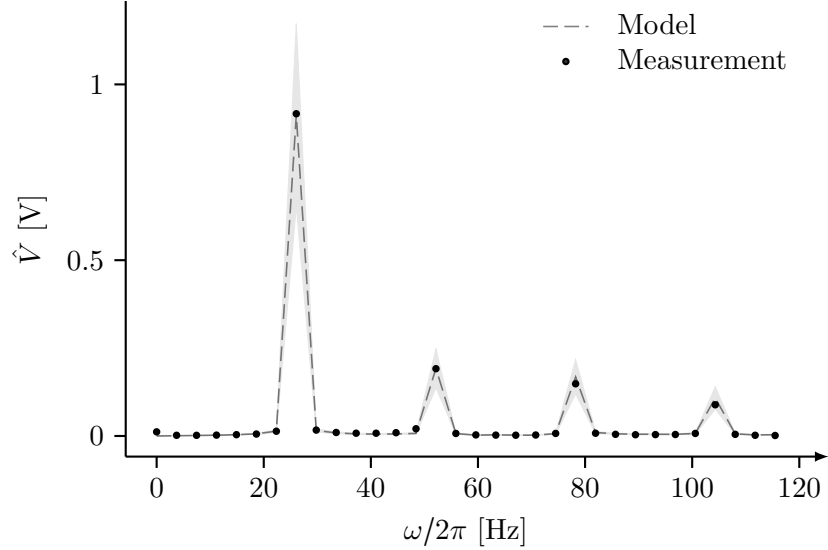


FIG. 6. Comparison of the model (analytical solution) and of the voltage measurements in the frequency space. Continuous line: Fourier transform of the voltage measurements, Dashed line: analytical expression of the voltage derived in Section III. Grey zone: error bars due to the uncertainty in the material’s parameter. Measurement performed at 26 Hz with 909 k Ω load on the 116 μm -thick sample.

to the power of $2/3$, plotted as a function of R , is shown in Figure 7 for different excitation frequencies: changing the frequency leads to different profiles. The same values plotted as a function of the product $R\omega$ is shown in Figure 8. The expected scaling law Eq. (16) is observed: all points measured at various frequencies collapse on the same curve.

This scaling law allows us to extract the value of the prefactor \mathcal{A} of Eq. (16) with a single one-parameter fit for the whole set of measurements when varying both the load resistances and frequencies.

D. Power

The power generated by the piezoelectric membrane is given by the product of the voltage by the current measured on the load resistance. The result is compared to Eq. (17) derived in §III C. As for the previous subsections, the data and the model are compared as a function of the resistance, and plotted in Fig. 9 for two different thicknesses of the PVDF film ($\ell = 116$ and $\ell = 12 \mu\text{m}$). Such a profile can be seen on various polymer systems in the literature¹⁶.

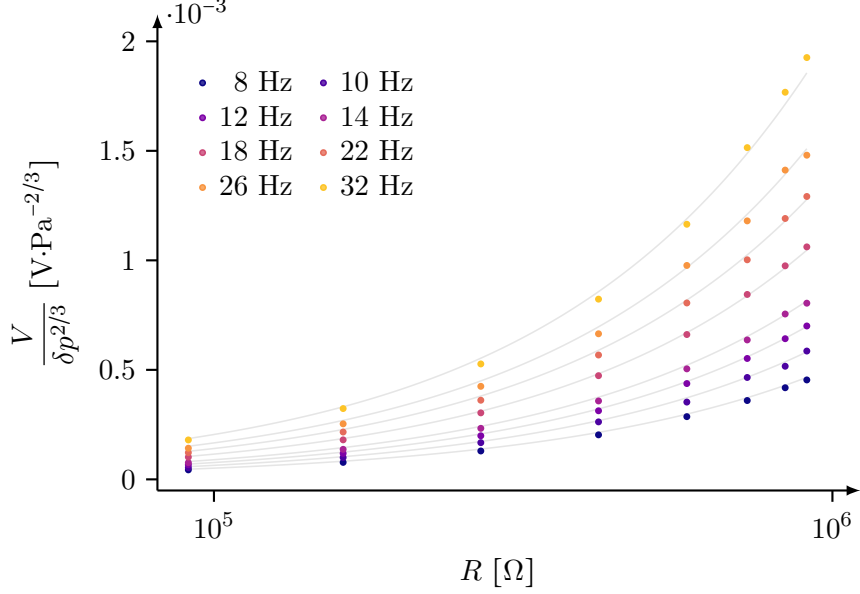


FIG. 7. First peak of the Fourier transform of the voltage divided by the pressure to the power of $2/3$ as a function of the effective resistance R . The grey lines are fit from Eq. (16) with the fitting parameter \mathcal{A} . Measurement performed on the $116 \mu\text{m}$ -thick sample.

The maxima (not reached by the experimental points due to the internal resistance of the ADC card) correspond to the impedance matching $RC\omega = 1$, as predicted in §III C. The load resistances range within $R_l \leq 10^7 \Omega$, but the measured points are confined to the region $R < 1 \text{ M}\Omega$ due to the limitation of the internal resistance of our voltmeter ($1 \text{ M}\Omega$).

E. Thickness dependence

Last but not least, the model can be challenged with the measurements performed on different membranes of various thicknesses, and plotted in a set of scaling laws (see Figure 10).

For the three thicknesses $\ell = 116$, $\ell = 28$ and $\ell = 12 \mu\text{m}$, the scaling law is fit as a function of the variable $R\omega$, with the parameter \mathcal{A} as a fitting parameter. The profile of \mathcal{A} as a function of the expected power law $\ell^{-2/3}$ (as shown in Eq. (16) is plotted in Fig. 11. The last value for $\ell = 12 \mu\text{m}$ is clearly beyond the error bar. This significant discrepancy may first be attributed to the limitation of the linear constitutive equations (limit of validity of Eq. (1)). However, this is probably not the case because we observed that the gold electrodes plays

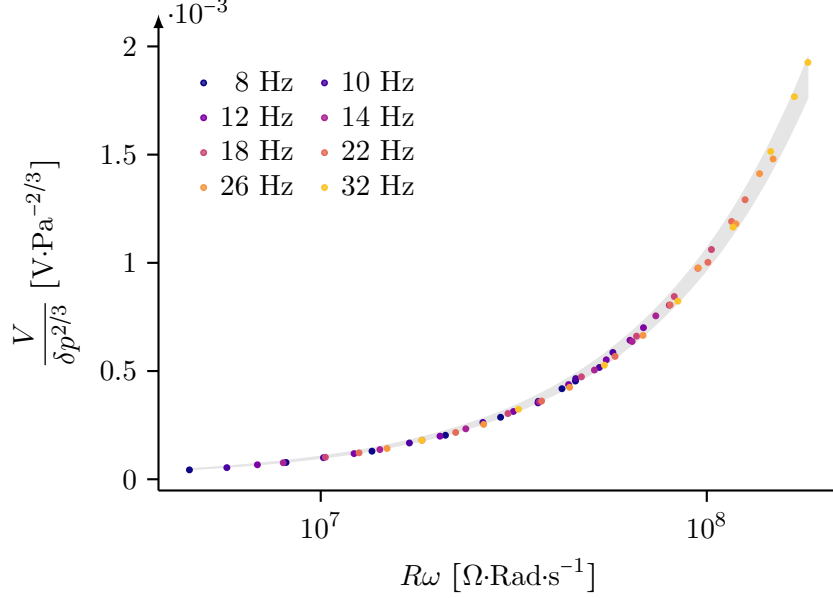


FIG. 8. First peak of the Fourier transform of the voltage divided by the pressure to the power of $2/3$ as a function of the product $R\omega$. The scaling law is observed. The grey line is fit from eq. (16) with the fitting parameter \mathcal{A} . Measurement performed on the $116 \mu\text{m}$ -thick sample.

a significant role in the voltage, that accounts for the deviation, as discussed below (last section and Appendix D). A forthcoming study about this effect appears necessary for a correct optimization of the piezogenerators obtained from thin films.

V. DISCUSSION AND CONCLUSION

We have studied theoretically and experimentally the large bending regime of piezoelectric generators based on polymer materials, and connected to a load circuit. The polymer film is free standing with a radial deformation (it is fixed by a radial ring at the border as depicted in Fig.1). The transverse displacement is large (several hundreds of microns), but nevertheless the linear constitutive equations of the Curie's brothers are assumed to be still valid (small strain). The large bending leads to a non-linear response of the voltage with respect to the over-pressure excitation δp . The measured power is of the order of $3\mu\text{W}$ for a thin PVDF film of $\ell = 30$ micron, of volume $10^{-9} m^3$. The power density per unit of volume is of the order of $3 \text{ kW}/m^3$, and the power density per unit of surface is of the order of $10 \text{ mW}/m^2$.

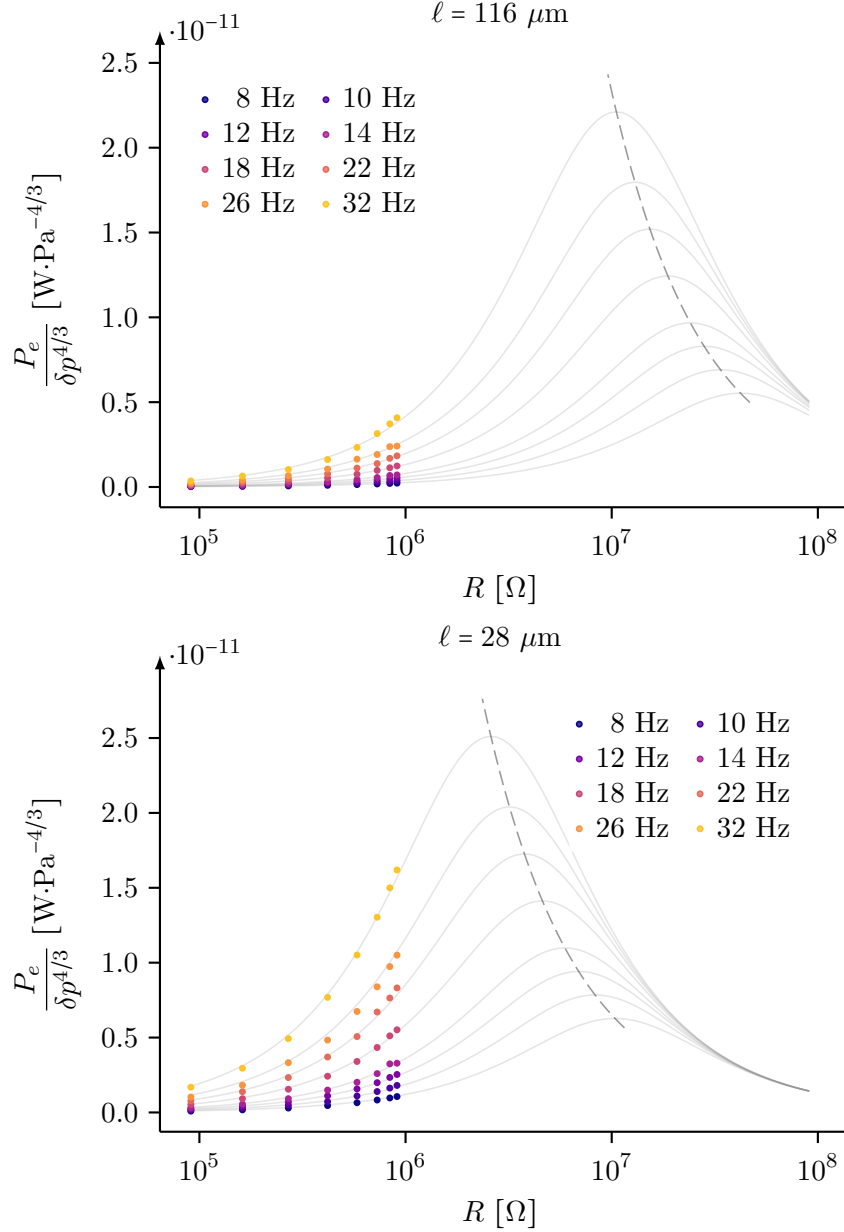


FIG. 9. Measured power as a function of the effective resistance R for different values of the load resistance R_l and excitation frequency ω . Grey dashed line: maxima at $\omega RC = 1$. Top: $\ell = 116 \mu m$. Bottom: $\ell = 28 \mu m$

An analytical model is developed in order to derive useful expressions of the Fourier transform of both the voltage and the power delivered in the load circuit.

Four main characteristics are predicted, that are 1) the well known maxima of the power imposed by the impedance matching condition ($RC\omega = 1$), 2) the $(\delta p^{2/3})_\omega$ dependence of the Fourier transform of the voltage with the over-pressure, 3) the power law dependence as

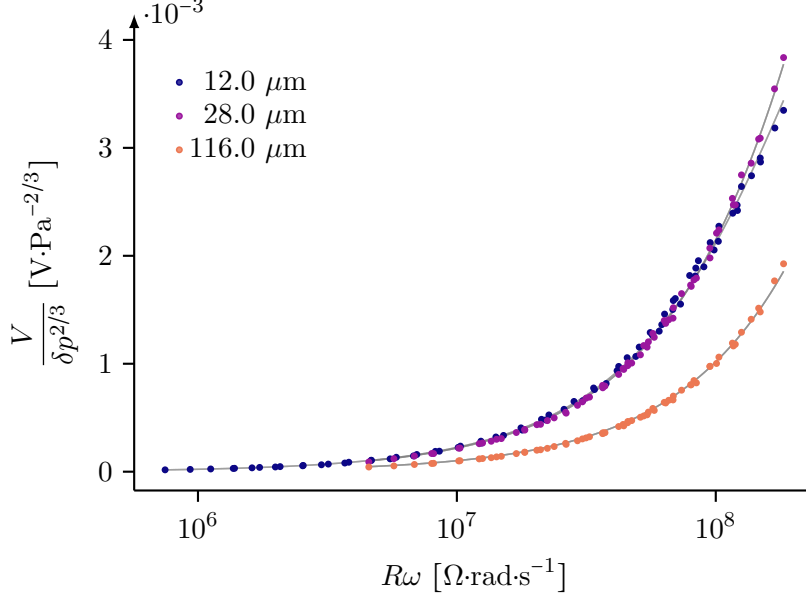


FIG. 10. Scaling law for the various membrane thicknesses.

a function of the product $R\omega$ of the ratio $V_\omega/(\delta p^{2/3})_\omega$, and 4) the dependence as a function of the thickness ℓ of the polymer film: $V_\omega(\ell) \propto \ell^{-2/3}$. The verification of this power law, presented in Fig. 11, shows a good quantitative agreement, except for the last point at thickness $\ell = 12 \mu\text{m}$. This discrepancy is attributed to the unexpected role of the electrode, which is significant only for thin films. Indeed, a correction can be performed according to the empirical fit deduced from the data shown in Fig. 12, after which the three points would be aligned in Fig. 11.

Besides, the efficiency of the generator can be calculated with various definitions¹⁷. Without going into the details, suffice to say that the maximum working condition is given by the relation $RC\omega = 1$ on the one hand, and on the other hand the maximum amplitude of the effect is obtained for material's parameters that maximize the product ($\mathcal{A}^2 \propto e_{31}^2 Y^{-2/3}$) (see eq. (15) and eq. (17)). This quantity, defined with intrinsic parameters of the material only, is of the order of the product of an effective piezoelectric coupling squared, \bar{d}^2 , times Young's modulus $Y^{2/3}$, where $\bar{d} = \frac{d_{31} + \nu d_{33}}{(1+\nu)(1-2\nu)} \left(3 \frac{1-\nu}{7-\nu}\right)^{2/3}$. The product $\bar{d}^2 Y^{2/3}$ acts here as the Figure of Merit of our generator, assuming a given external mechanical excitation. It is worth pointing out that the electric permittivity, which only appears in the expression of C , does not participate in this Figure of Merit. More precisely, the permittivity has to be tuned independently in order to fit the maximum power condition $RC\omega = 1$.

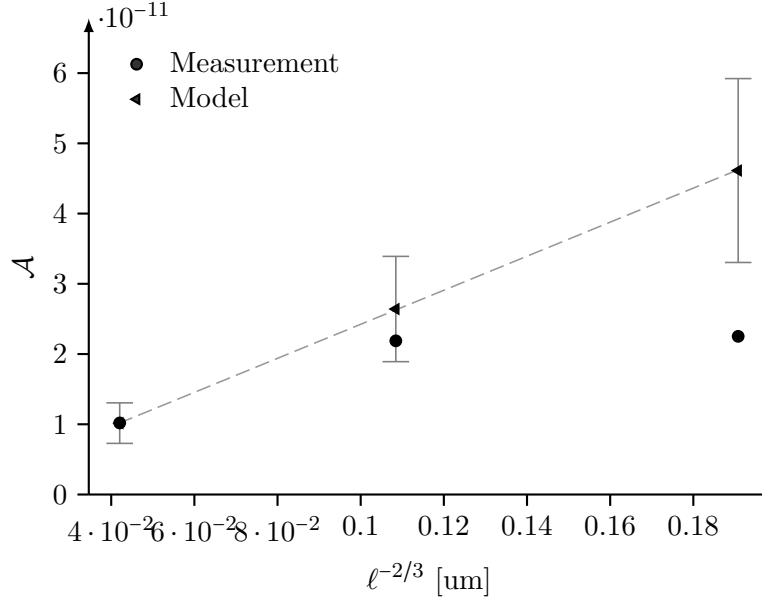


FIG. 11. Prefactor \mathcal{A} of the voltage V as a function of the membrane thickness ℓ . The deviation between the model and the data for the point corresponding to the smaller thickness $\ell = 12$ is due to the Au electrode (see text).

ACKNOWLEDGMENTS

This work was supported by the grant NanoVIBES (Labex NanoSaclay, reference: ANR-10-LABX-0035). The authors wish to specially thank Noelle Gogneau from C2N (UMR 9001) Palaiseau, France, for coordinating NanoVIBES project.

VI. CONFLICT OF INTEREST

The authors have no conflicts to disclose

VII. DATA AVAILABILITY

All data measured during this study are available from the corresponding author upon reasonable request.

Appendix A: Au-sputtered PVDF Membrane specifications

The 50 nm-thick gold electrodes were sputtered with a Turbomolecular pumped coater (Quorum Q150TS) on each side of the PVDF films. To adapt the geometry of the gold layers (yellow area in Fig.1) to the positions of the electric contacts in the measurement chamber, a specific home-made mask was designed. We use typically 200 seconds duration of the deposition for 50 nm-thick gold layer.

The piezoelectric PVDF films were purchased from GoodFellow manufacturer. Most of the intrinsic parameters were extracted from the manufacturer GoodFellow technical datasheet except the thicknesses and the dielectric permittivity that were respectively measured using FTIR spectroscopy and a Novocontrol broad band dielectric spectrometer. Their characteristics are: thickness $\ell = \{0.01, 0.028, 0.11\}$ mm, orientation: uni-axially oriented, transparency: clear/transparent.

$$d_{33} : 16 \cdot 10^{-12} \pm 10\% \text{ C/N}$$

$$d_{3t} : 3.5 \cdot 10^{-12} \pm 10\% \text{ C/N}$$

$$\ell : 12, 28 \text{ and } 116 \mu\text{m}$$

$$\epsilon_{33} : 1.15 \cdot 10^{-10} \pm 10\% \text{ at } 12 \mu\text{m}$$

$$\epsilon_{33} : 1.42 \cdot 10^{-10} \pm 10\% \text{ at } 28 \mu\text{m}$$

$$\epsilon_{33} : 1.46 \cdot 10^{-10} \pm 10\% \text{ at } 116 \mu\text{m}$$

$$\text{Young's modulus } Y : 3.2 \text{ GPa}$$

$$\text{Poisson's ratio } \nu : 0.34$$

$$\text{Gold electrode area } A_e : 3.75 \text{ cm}^2$$

$$\text{Pressurized area } A_p : 0.5 \text{ cm}^2$$

These parameters allow to check quantitatively the validity of the model described in section III, in particular the validity of the small strain, and that the displacement amplitude remains within the range allowed by the model, as shown in Table I.

thickness ℓ [μm]	12	28	116
$\frac{w_{max}}{2} \sqrt{\frac{\pi}{A_p}}$ [%]	7.95	6.00	3.73
$\frac{w_{max}}{\ell}$ [-]	53.0	17.1	2.6
S_{max} [%]	1.68	0.96	0.37

TABLE I. For different membrane thicknesses ℓ , comparison of the maximum transverse displacement and the membrane radius (row 2), or thickness (row 3), and maximum strain (row 4).

Appendix B: The effect of the electrodes

The observation of the dependence of the piezoelectric voltage to the electrode, as shown in Fig. 12, was a surprise. This means that the measured voltage should be corrected from the (unknown) effect of the gold electrodes, in order to take into account only the piezoelectric contribution. The correction depends on the relative thickness of the Au electrode, with respect to the thickness ℓ of the film. Note that the effect of the electrode thickness was already experimentally observed e.g. by Zhang et al.¹⁸.

The effect of the electrode is negligible for thick films, but it becomes significant for the 12 μm thick film. This contribution explains the quantitative deviation observed in Fig. 11, between the measured raw data and the model.

1. Averaged value of d_{3t} in the case of transverse isotropy

As far as the specifications are concerned, the piezoelectric coupling \mathfrak{d} is given by the strain-charge law:

$$\begin{cases} \mathbf{S} = \mathbb{C}_E^{-1} \cdot \mathbf{T} + \mathfrak{d}^T \cdot \mathbf{E} \\ \mathbf{D} = \mathfrak{d} \cdot \mathbf{T} + \epsilon_T \cdot \mathbf{E} \end{cases} \quad (\text{B1})$$

Nevertheless, the values provided by the manufacturer give both d_{31} and d_{32} components, consequence of the local texture. Yet, on our scale, the membrane is transversely isotropic,

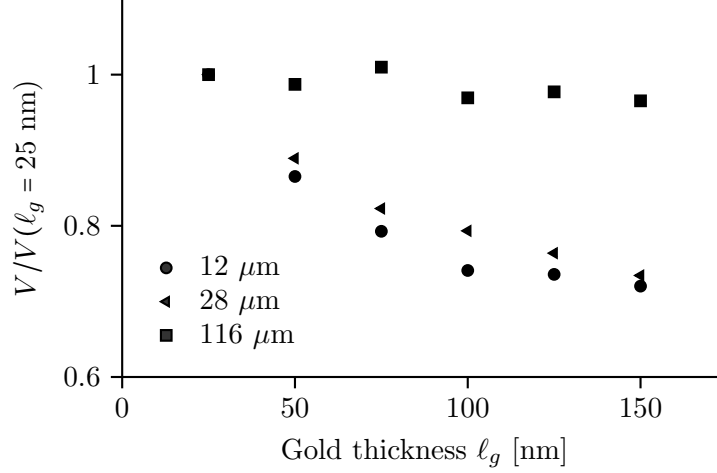


FIG. 12. Effect of the gold electrodes thickness on the prefactor \mathcal{A} measured by fitting the scaling law

requiring to average both quantities into one single coupling factor d_{3t} .

For a uniaxial stress field of magnitude T_0 along any given direction \mathbf{e} in the membrane plane $(\mathbf{i}_1, \mathbf{i}_2)$, where

$$\mathbf{e} = \cos \phi \mathbf{i}_1 + \sin \phi \mathbf{i}_2$$

the tensor expression of the stress is:

$$\begin{aligned} \mathbb{T} &= T_0 \mathbf{e} \otimes \mathbf{e} \\ &= T_0 \left[\begin{array}{c} \cos^2 \phi \mathbf{i}_1 \otimes \mathbf{i}_1 + \sin^2 \phi \mathbf{i}_2 \otimes \mathbf{i}_2 \\ + \cos \phi \sin \phi (\mathbf{i}_1 \otimes \mathbf{i}_2 + \mathbf{i}_2 \otimes \mathbf{i}_1) \end{array} \right] \end{aligned} \quad (\text{B2})$$

Taking into account the non null components in the case of transverse isotropy, the average effective piezoelectric coefficients are then computed from:

$$D_z = T_0 (d_{31} \cos^2 \phi + d_{32} \sin^2 \phi) + \epsilon_{33} E_z \quad (\text{B3})$$

Hence, the effective piezoelectric coefficient is given by:

$$\begin{aligned} \tilde{d}_{3t} &= \frac{1}{2\pi} \int_0^{2\pi} (d_{31} \cos^2 \phi + d_{32} \sin^2 \phi) d\phi \\ &= \frac{d_{31} + d_{32}}{2}. \end{aligned} \quad (\text{B4})$$

where t refers to any in-plane direction.

Appendix C: Direct evidence of the $\delta p^{2/3}$ dependence

If the pressure excitation is performed with valve contacted to a pressurized tank, so that the pressure time-dependence is a step function, the maximum voltage peak follows a clear $\delta p^{3/2}$ dependence, as shown in the Fig. 13 below. The measurements were previously performed for various nanostructured piezoelectric PVDF and composite films, with e-beam irradiations of different doses with the idea to soften the materials by inducing chain scissions (as detailed in the inset for the different symbols). The study is published in the reference¹⁹, however no interpretation was reported about the observed empirical power law depicting $V = f(\delta p)$.

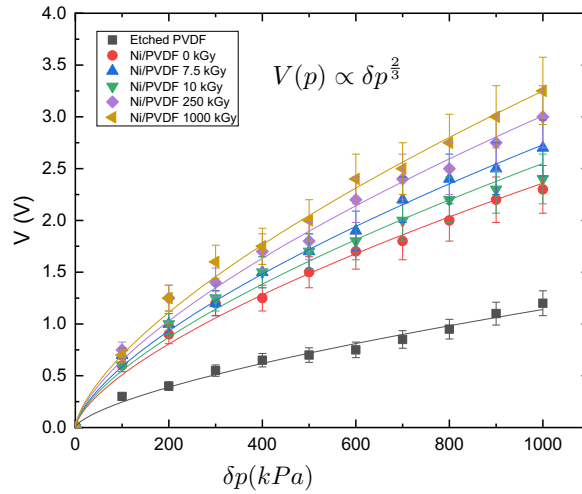


FIG. 13. Maximum piezoelectric voltage as a function of the overpressure resulting from a stepwise time-dependence excitation - raw data obtained for nanostructured piezoelectric PVDF and composite films with different irradiation treatment were extracted from reference¹⁹. The lines corresponds to power laws $\delta p^{2/3}$. Measurement performed on 10 μm thick film.

* jean-eric.wegrowe@polytechnique.edu

¹ Stephen P. Timoshenko and S Woinowsky-Krieger, “Theory of plates and shells,” (1959).

² Bert A. Auld, “Acoustic fields and waves in solids,” (McGraw-Hill, 1973).

- ³ Changki Mo, Joseph Davidson, and William W Clark, “Energy harvesting with piezoelectric circular membrane under pressure loading,” *Smart Materials and Structures* **23**, 045005 (2014).
- ⁴ Xinyue Wang, Jialin Zuo, Tianlin Jiang, Jinxin Xiao, Jie Tong, Shiqing Huang, and Wenhua Zhang, “Analysis of vibration electromechanical response behavior of poly(vinylidene fluoride) piezoelectric films,” *Energies* **17** (2024), 10.3390/en17163886.
- ⁵ Anna A. Dedkova, Petr Yu. Glagolev, Gleb D. Demin, Evgeney E. Gusev, and Pavel A. Skvortsov, “Mechanical stresses analysis of thin round membranes in the case of large deflections,” in *2020 IEEE Conference of Russian Young Researchers in Electrical and Electronic Engineering (EIConRus)* (2020) pp. 2288–2292.
- ⁶ Abhishek Sasmal, Jaganathan Senthilnathan, Arunachalakasi Arockiarajan, and Masahiro Yoshimura, “Two-dimensional metal-organic framework incorporated highly polar pvdf for dielectric energy storage and mechanical energy harvesting,” *Nanomaterials* **13** (2023), 10.3390/nano13061098.
- ⁷ Naval Sourav, Verma Pratibha, Jain Ankesh, and Mallick Dhiman, “Hybrid vector and pressure sensor for fingertip dynamics sensing using dc-triboelectric/ac-piezoelectric mechanisms,” *Sensors and Actuators A: Physical* **355**, 114330 (2023).
- ⁸ Wang Sasa, Khan Asif Abdullah, Teale Sam, Xu Jian, H. Parmar Darshan, Zhao Ruyan, Grater Luke, Serles Peter, Zou Yu, Filleter Tobin, S. Seferos Dwight, Ban Dayan, and H. Sargent Edward, “Large piezoelectric response in a jahn-teller distorted molecular metal halide,” *Nature Communications* volume **14**, 1852 (2023).
- ⁹ Morteza Hassanpour Amiri, Rose Fatscher, Rebecca Taylor, Paulo R.F. Rocha, Chris R. Bowen, and Kamal Asadi, “Piezoelectric energy harvesters: A critical assessment and a standardized reporting of power-producing vibrational harvesters,” *Nano Energy* **106**, 108073 (2023).
- ¹⁰ Daniella B. Deutz, John-Alan Pascoe, Ben Schelen, Sybrand van der Zwaag, Dago M. de Leeuw, and Pim Groen, “Analysis and experimental validation of the figure of merit for piezoelectric energy harvesters,” *Mater. Horiz.* **5**, 444–453 (2018).
- ¹¹ Michaël Peigney and Dominique Siegert, “Piezoelectric energy harvesting from traffic-induced bridge vibrations,” *Smart Materials and Structures* **22**, 095019 (2013).
- ¹² Zihe Li, James Roscow, Hamideh Khanbareh, Geoff Haswell, and Chris Bowen, “Energy harvesting from water flow by using piezoelectric materials,” *Advanced Energy and Sustainability Research* **5**, 2300235 (2024), <https://onlinelibrary.wiley.com/doi/pdf/10.1002/aesr.202300235>.

- ¹³ Jonathan Granstrom, Joel Feenstra, Henry A Sodano, and Kevin Farinholt, “Energy harvesting from a backpack instrumented with piezoelectric shoulder straps,” *Smart Materials and Structures* **16**, 1810 (2007).
- ¹⁴ Erik Nilsson, Anja Lund, Christian Jonasson, Christer Johansson, and Bengt Hagström, “Poling and characterization of piezoelectric polymer fibers for use in textile sensors,” *Sensors and Actuators A: Physical* **201**, 477–486 (2013).
- ¹⁵ IEEE, “Publication and proposed revision of ansi/ieee standard 176-1987 ”ansi/ieee standard on piezoelectricity”,” *IEEE Transactions on Ultrasonics, Ferroelectrics, and Frequency Control* **43**, 717– (1996).
- ¹⁶ Chang Kyu Jeong, Changyeon Baek, Angus I. Kingon, Kwi-Il Park, and Seung-Hyun Kim, “Lead-free perovskite nanowire-employed piezopolymer for highly efficient flexible nanocomposite energy harvester,” *Small* **14**, 1704022 (2018), <https://onlinelibrary.wiley.com/doi/pdf/10.1002/sml.201704022>.
- ¹⁷ Kenji Uchino, “Piezoelectric energy harvesting systems - essentials to successful developments,” *Energy Technology* **6**, 829–848 (2018), <https://onlinelibrary.wiley.com/doi/pdf/10.1002/ente.201700785>.
- ¹⁸ Lei Zhang, Sharon Roslyn Oh, Ting Chong Wong, Chin Yaw Tan, and Kui Yao, “Piezoelectric polymer multilayer on flexible substrate for energy harvesting,” *IEEE Transactions on Ultrasonics, Ferroelectrics, and Frequency Control* **60**, 2013–2020 (2013).
- ¹⁹ Natalia Potrzebowska, Olivier Cavani, Ozlem Oral, Olivier Doaré, Giuseppe Melilli, Jean-Eric Wegrowe, and Marie-Claude. Clochard, “Mixing nanostructured ni/piezopvdf composite thin films with e-beam irradiation: A beneficial synergy to piezoelectric response,” *Materials Today Communications* **28**, 102528 (2021).